A Local Alumina and ACD Observer for Aluminium Electrolysis Cells Using Anode Currents

Andrea Mattioni[1], Lucas Jose da Silva Moreira[2], Gildas Besançon[3], Mirko Fiacchini[4] and Hervé Roustan[5]
1. Post-doc
3. Full Professor
4. Associate Professor
Université Grenoble Alpes, CNRS, Grenoble INP, GIPSA-Lab, Grenoble, France
2. Graduate R&D Process Control
5. Solutions Technologies Aluminium Expert
Rio Tinto, Saint-Jean-de-Maurienne, France
Corresponding author: lucasjose.dasilvamoreira@riotinto.com
https://doi.org/10.71659/icsoba2024-al016

Abstract

In industrial aluminium electrolysis cells, the distribution of alumina is often non-uniform. This can be attributed to several factors, such as bath movement, discrepancies in alumina feeding from different feeders and variations in consumption rates, to name a few. Furthermore, the non-uniform distribution of alumina has some effect on the pseudo-resistance of the cell and its variability, which are typically used to control alumina concentration in the cell. However, this can lead to an unpredictable lack of alumina locally in the cell, resulting in localized anode effects that can transform into generalized anode effects. Therefore, to achieve an independent utilization of the feeders for balancing the alumina distribution in the cell, the first step is to have a reliable estimate of the alumina distribution. To realize it, distributed information, such as the anode currents, is required. This study uses a two-step approach for estimating local alumina concentration and anode-cathode distance (ACD). In the first step, an observer uses the cell pseudo-resistance to obtain an initial estimation of alumina concentration and ACD. In the second step, a second observer uses the individual anode currents to correct the initial estimations. This paper is focused on the design of the observers and the required signal processing to obtain reliable estimations. Finally, the proposed method is validated with data from a smelter.

Keywords: Aluminium reduction cells, Alumina concentration, Cell pseudo-resistance monitoring, Observer design, Filtering and estimation.

1. Introduction

In the last twenty years, one of the main objectives of the aluminium industry has been to decrease the greenhouse gas emissions. In aluminium production, a large part of the total greenhouse gas emissions comes from anode effects. When alumina concentration goes under a certain threshold, a more energy-demanding chemical reaction involving the emissions of CF_4 becomes dominant [1]. Moreover, aluminium reduction cells can have significant alumina concentration gradients [2], leading to anode effects starting from a deficit alumina concentration under one or few anodes. The reduction of this phenomenon requires a better control of the alumina feeding: instead of a uniform feeding within the cell, areas with less alumina concentration can be targeted to receive a bigger alumina feeding. The first step for a better alumina feeding distribution is to have an estimation of the alumina concentration gradient in the cell. In this paper, we propose a distributed observer that makes use of the anode currents to estimate the local dissolved alumina and ACD under the anodes.

In the last decade, observers based on a discretized cell model have been proposed for the estimation of the dissolved alumina concentration distribution. In [3], a multi-level Extended Kalman Filter (EKF) for the estimation of local dissolved alumina and ACD, based on discretized cell models, has been proposed. In [4] the authors propose an Iterated EKF that, together with local dissolved alumina and ACD, estimates the bath flow. In [5], the authors proposed a control scheme for the feeder individualization that includes an LQR control based on a EKF distributed alumina estimation. In [6] the authors used a Huber function based Kalman Filter to estimate the local dissolved alumina and ACD.

The common point between the previous estimation algorithms resides in the fact that the anode currents have been used only as input to the discretized cell model, and not to correct the estimation in the observer algorithm. To use the anode currents in the observer algorithm, in continuity with the work proposed in [3-6], a possibility would be to derive an explicit expression of the anode currents, starting from – an affine with respect to the anode current – simplified expression of the voltage. Even though this is the most academically sound solution, some application drawbacks prevent us to use this method: dealing with different anode currents noise, unavailability (or excessive noise) of one or some anode current signals requires the design of a completely new observer, and the sensitivity to non-modelled behaviours becomes difficult to manage with many outputs.

In this work, we propose a two-stage algorithm for estimating local dissolved alumina concentration and ACD. The first stage involves the observer presented in [7], which utilizes the cell pseudo-resistance to estimate *instrumental* dissolved alumina and *instrumental* ACD. The second stage comprises several anode observers equal to the number of available anode currents, which use the anode pseudo-resistance to refine the instrumental estimations from the first stage, thereby obtaining the local dissolved alumina and ACD. The paper is organized as follows: in Section 2 we present the essential information regarding the *instrumental* observer; in Section 3 we show the necessary current pre-processing to apply the local observer that is presented in Section 4; the application of the local observer on industrial data is given at the end of Section 4; finally, some concluding remarks and possible future developments are given in Section 5.

2. Instrumental Alumina Observer

The first stage of anode dissolved alumina estimation consists of the observer of the *instrumental* dissolved alumina $w_d(k)$ and *instrumental* $ACD(k)$. As shown in Figure 1, the observer consists of an algorithm that takes as input the feeding period, the line current and the measured pseudo-resistance and returns the *instrumental* dissolved and sludge alumina together with the *instrumental* ACD.

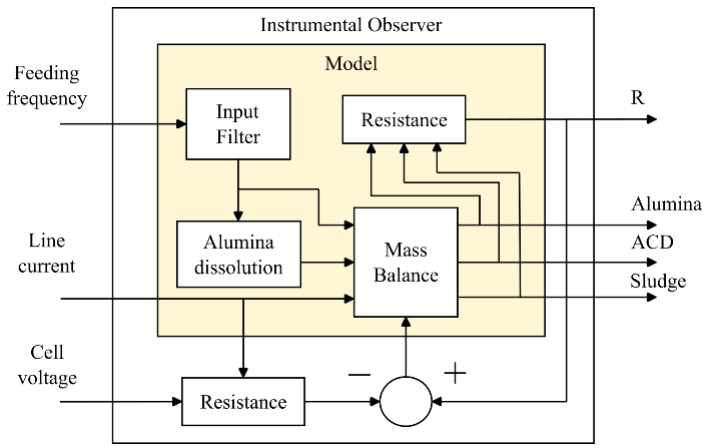

Figure 1. Schematic representation of the *instrumental* observer.

It is worth remarking that the word *instrumental* has been used on purpose: the observer estimated quantities do not correspond to the average alumina concentration and average ACD but to the estimated quantities as if the cell was a single anode cell of infinitesimally small dimensions. As shown in Figure 1, the estimator model is composed by four different blocks: input filter, alumina dissolution, mass balance and resistance calculation. For a through explanation of every and each of the previous blocks, we refer the reader to [7].

2.1 Model and Recursive Equations

Considering a sampling period of $dt = 1\ s$, the observer equations in [7] can be discretized as proposed in this section. Firstly, we introduce the feeding frequency $F(k)$ input filter:

$$\begin{cases} x_1(k+1) = (1 - 2\tau(k)dt)x_1(k) - \tau(k)^2 dt x_2(k) + \tau(k)^2 dt F(k) \\ x_2(k+1) = x_2(k) + dt x_1(k) \\ u_1(k) = x_2(k). \end{cases} \quad (1)$$

with:

$$\tau(k) = \frac{11}{10}F(k) + 0.00865 \quad (2)$$

and where:

x_1, x_2	Filter states
τ	Filter parameter
u_1	Effective feeding frequency.

Secondly, the alumina dissolution model:

$$\begin{cases} w_{ud,f}(k+1) = \left(1 - dt\ k_{d,f}\right)w_{ud,f}(k) + dt\ r_f \alpha_2(k) u_1(k) \\ w_{ud,s}(k+1) = \left(1 - dt\ k_{d,s}\right)w_{ud,s}(k) + dt\ r_s \alpha_2(k) u_1(k) \\ u_2(k) = k_{d,f} w_{ud,f}(k) + k_{d,s} w_{ud,s}(k), \end{cases} \quad (3)$$

with:

$$\alpha_2(k) = \frac{10^2 m_{in} n_F(k)}{M_{bath}} \quad (4)$$

and where:

$w_{ud,f}$	Fast undissolved alumina	$r_s = 0.75$	Per unit slow diss. alumina
$w_{ud,s}$	Slow undissolved alumina	m_{in}	Dose mass, kg
$k_{d,f} = 0.001$	Fast dissolution coefficient	n_F	Number of active feeders
$k_{d,s} = 0.005$	Slow dissolution coefficient	M_{bath}	Total bath mass, kg.
$r_f = 0.25$	Per unit fast diss alumina		

Thirdly, the mass balance equation with the addition of the sludge alumina state to account for the resistance hysteresis behaviour [8]:

$$\begin{cases} \widehat{w}_d(k+1) = \widehat{w}_d(k) - dt\ \alpha_1 I_{line}(k) + dt\ u_2(k) \\ \widehat{ACD}(k+1) = \widehat{ACD}(k) - dt\ \alpha_3\ I_{line}(k) + dt\ bm(k) \\ \widehat{w}_{sl}(k+1) = (1 - dt\ k_{sl})\widehat{w}_{sl}(k) + dt\ r_{sl}\alpha_2(k)u_1(k) \\ \hat{R}(k) = \frac{k_1}{\widehat{w}_d(k) - w_{ae}} + k_2 \widehat{w}_d(k) + k_3 \widehat{ACD}(k) + k_4 + k_5(\widehat{w}_{sl}(k) - w_{sl}^*) \end{cases} \quad (5)$$

where:

$\widehat{w}_d$	*Instrumental* diss alumina, %	$\hat{R}$	Estimated pseudo-resistance, Ω
$\widehat{ACD}$	*Instrumental* ACD, cm	k_i	$\hat{R}$ parameters
$\widehat{w}_{sl}$	Sludge alumina, %	$k_{sl} = 0.0007$	$\widehat{w}_{sl}$ Dissolution constant
I_{line}	Line current, A	$r_{sl} = 0.001$	Per unit $\widehat{w}_{sl}$ injection.
bm	Beam movement, cm/s		

For the definition of the $k_i,\ i = \{1, \dots, 5\}$ parameters we refer to Section 2.3 of [7]. The α_1 and α_3 parameters are defined as:

$$\alpha_1 = \frac{10^2 Al_2O_{3,m} C_e}{6\mathcal{F} M_{bath}} \qquad \alpha_3 = \frac{C_e}{S\mathcal{F}}\left(\frac{Al_m}{3\rho_{Al}} - \frac{C_m}{4\rho_C}\right) \tag{6}$$

where:

$Al_2O_{3,m} = 0.10196$	Alumina molar mass, kg/mol
$\mathcal{F} = 96485$	Faraday constant, s·A/mol
C_e	Current efficiency, %
S	Average bath surface, cm²
$Al_m = 0.02698$	Aluminium molar mass, kg/mol
$\rho_{Al} = 0.002375$	Aluminium density, kg/cm^3
$C_m = 0.01201$	Carbon molar mass, kg/mol
$\rho_C = 0.0016$	Carbon density, kg/cm^3.

To design the observer, we make a change of coordinates: we replace the variable $\widehat{w}_d$ with the resistance $\hat{R}$ in the dynamic equations. In the new coordinates $\hat{x} = \left[\hat{R}, \widehat{ACD}, \widehat{w}_{sl}\right]^T$, the dynamics equations can be written in the following form:

$$\begin{cases} \hat{x}(k+1) = A\hat{x}(k) + Bu(k) + f(\hat{x}(k), u(k)) \\ \hat{R}(k) = C\hat{x}(k) \\ \widehat{w}_d(k) = \frac{1}{2k_2}\left(V_1\hat{x}(k) + c_1 - \sqrt{\hat{x}(k)^T M\hat{x}(k) + V_2\hat{x}(k) + c_2}\right) \end{cases} \tag{7}$$

where:

$$A = \begin{bmatrix} 1 & 0 & -dt\ k_{sl}\ k_5 \\ 0 & 1 & 0 \\ 0 & 0 & 1 - dtk_{sl} \end{bmatrix} \quad u(k) = \begin{bmatrix} u_1(k) \\ u_2(k) \\ I_{line}(k) \\ bm(k) \end{bmatrix} \quad f(\hat{x}, u) = \begin{bmatrix} -\dfrac{dtk_1}{(w_d - w_{ae})^2}(u_2 - \alpha_1 I_{line}) \\ 0 \\ 0 \end{bmatrix}$$

$$B = \begin{bmatrix} dt\ r_{sl}\ k_5\ \alpha_2 & dt\ k_2 & -dt(\alpha_1 k_2 + \alpha_3 k_3) & dt\ k_3 \\ 0 & 0 & -dt\ \alpha_3 & dt \\ dt\ r_{sl}\ \alpha_2 & 0 & 0 & 0 \end{bmatrix} \quad C = [1 \quad 0 \quad 0] \tag{8}$$

$$V_1 = \begin{bmatrix} 1 \\ -k_3 \\ -k_5 \end{bmatrix}^T \quad V_2 = \begin{bmatrix} -2k_4 - 2k_2 w_{ae} \\ 2k_3k_4 + 2k_2k_3w_{ae} \\ 2k_4k_5 + 2k_2k_5w_{ae} \end{bmatrix}^T \quad M = \begin{bmatrix} 1 & -k_3 & -k_5 \\ -k_3 & k_3^2 & k_3k_5 \\ -k_5 & k_3k_5 & k_5^2 \end{bmatrix}$$

$$c_1 = -k_4 + k_2 w_{ae} \qquad c_2 = k_4^2 + (k_2 w_{ae})^2 + 2k_2k_4w_{ae} - 4k_1k_2.$$

The *instrumental* observer is obtained applying the Extended Kalman Filter algorithm to system (7). This observer is based on the mass balance equations describing the aluminium electrolysis reaction that consumes alumina and carbon to produce aluminium. Therefore, when the cell does not behave as in the nominal case, the estimation is not reliable anymore [7]. It is for this reason that the proposed observer must be suspended during anode change, tapping and anode effect.

Moreover, as explained in [7], the algorithm convergence to plausible estimations is approximately 40 minutes.

3. Current Signal Processing and Testing

To estimate the alumina concentration using a model-based observer, the first step is to process the anode current signals eliminating the non-modelled behaviours and exclude the too noisy ones. The most important non-modelled behaviours that can affect the alumina estimation are the following: anode slots disappearance, anode currents change in anodes next to the new anodes, anode slippage. In what follows, we address these non-modelled behaviours, specifying the frequency at which they impact the corresponding anode current. Subsequently, we introduce a specific pre-processing technique for the anode currents to mitigate these unmodeled effects.

Anode slots disappearance
The main role of anode slots is to evacuate the gas (mainly CO_2) created from the electrolysis reaction. The gas layer under the anode is responsible for a part of the anode resistance: the thicker the layer of gas, the higher the anode resistance. The anode slots evacuate a portion of these bubbles, enabling a thinner bubble layer compared to the unslotted case. In [9] the authors have shown that in the Alcoa smelters, the voltage drop due to the gas decreased from 0.24 V for non-slotted anodes to 0.08 for slotted ones. As shown in Figure 2, slots are continuously consumed, and the originally slotted anodes gradually transform into unslotted ones. In this paper, we assume that the transformation from slotted to unslotted (Figure 2(b) to Figure 2(c)) is reflected on an anode current rate with an associated frequency of 0.000023 Hz. On the other hand, in [10] the authors estimated that the fluctuation of anode current due to bubbles creation and release is at around 50 Hz. In our case, since the anode current sampling frequency is 1 Hz, the fluctuation due to bubble appearance and disappearance transforms into signal noise.

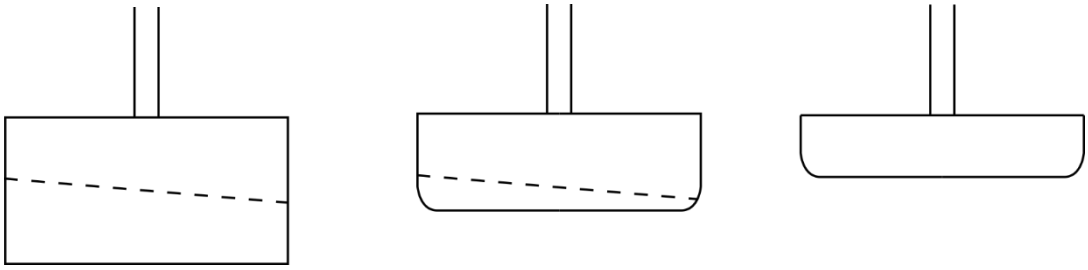

Figure 2. Representation of the anode consumption with respect to its slots.

Anode currents change in anodes next to the new anodes
In Figure 3, the currents of three anodes positioned nearby and three anodes situated farther away from a new anode are displayed. It can be observed that only the anodes next to the new anode experience a current increase. There is not a clear physical explanation to this phenomenon, but in this paper, we assume that the cause cannot be attributed to the alumina concentration. After carefully considering the current rate of change in this scenario based on available data, we suggest in this paper that the frequency associated with this phenomenon is 0.00007 Hz.

Anode slippage
Anode slippage can be caused by loose clamp or can happen accidentally during beam raising. This result to a slide down in the perpendicular direction of the anode, diminishing its ACD and therefore its bath resistance. The sudden resistance decrease transforms into a sudden current increase [11]. In this case the rate of change is 1 kA/min = 0.0166 Hz.

3.1 High-Pass Filter for Anode Currents

To reject the anode slot disappearance low-frequency component together with the anode current change in anodes next to new anodes, we design a High-pass filter. First, we define the measured anode current from the i-th anode as $I_i(t)$. From now on, the processed version of a raw current signal is identified with an overline on it, i.e., the processed version of $I_i(t)$ is identified with $\bar{I}_i(t)$. The processed i-th anode current is defined as the sum of a high frequency and a low-frequency components:

$$\bar{I}_i(t) = \bar{I}_{hf,i}(t) + \bar{I}_{pc,i}(t). \tag{9}$$

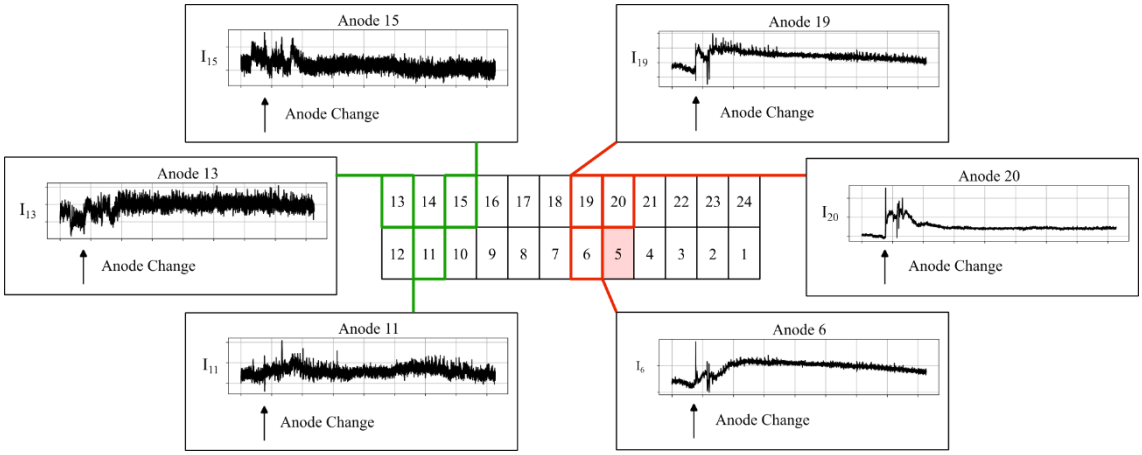

Figure 3. Anode currents behavior after the change of anode 5. Anodes 6, 19, 20, experience a sudden current increase followed by a slow decrease. Anodes 11, 13, 15 do not register this phenomenon.

The high-frequency component is obtained using a basic high-pass filter with a cut-off frequency of $f_{hf} = 0.0001$. In particular, the filter recursive equation writes:

$$\bar{I}_{hf,i}(k) = \alpha_{hf}\bar{I}_{hf,i}(k-1) + \alpha_{hf}\big(I_i(k) - I_i(k-1)\big), \tag{10}$$

where $\alpha_{hf} = \frac{1}{2\pi f_{hf}+1}$. The signal $\bar{I}_{pc,i}(t)$ is designed to be a piecewise continuous signal that update every time one of the following conditions happens: the end of an anode change, the end of an anode effect, the end of a tapping, the end of a line current change or every time two hours have passed. We name k^* the instant of time when one of the previous conditions is valid. The piecewise continuous current $\bar{I}_{pc,i}(k)$ is updated at k^* using the average of the last 60 values of $I_i(t)$:

$$\bar{I}_{pc,i}(k^*) = \frac{1}{60}\sum_{j=k-60}^{k} I_i(j). \tag{11}$$

It is worth noting that only the variations in $\bar{I}_{hf,i}(t)$ will be processed in the anode observer to be imputed to an anode dissolved alumina or anode ACD variation. On the other hand, variation of $\bar{I}_{pc,i}(t)$ will be solely imputed to the ACD. The downside of this decision is that ACD will incorporate all the pseudo-resistance variations that we estimate are not attributable to an alumina variation. To emphasize this concept, in the subsequent sections, we will refer to the estimated ACD of the i-th anode as the i-th pseudo-ACD.

3.2 Variance Real-Time Computation

To exclude from estimation the too noisy currents we design a real-time variance calculator: when a certain anode current variance exceeds the threshold, this anode current is excluded. We define with $V_{I,i}(k)$ the low pass filtrated variance of the i-th anode current at the k-th istant of time. The variable $\mu_{I,i}(k)$ represent the low-pass filtrated mean of the i-th anode current at the k-th instant of time. To compute this quantity in a recursive way, we propose the following update laws:

$$\begin{cases} \mu_{I,i}(k) = \mu_{I,i}(k-1) + 0.003(I_i(k) - \mu_{I,i}(k-1)) \\ V_{I,i}(k) = V_{I,i}(k-1) + 0.03\left(\left(I_i(k) - \mu_{I,i}(k-1)\right)^2 - V_{I,i}(k-1)\right). \end{cases} \quad (12)$$

We consider that the i-th current $I_i(k)$ is acceptable if its variance is lower than $1\ kA$. Hence, once the estimated filtered variance of the i-th anode $V_{I,i}(k)$ exceeds a certain threshold, the i-th current is deemed unusable.

3.3 Pass-Band Filter for Anode Slippage

To recognize when a possible anode slippage is taking place for a certain anode, we propose the implementation of a pass band filter. Here we present the recursive equations of the pass band filter:

$$\begin{cases} x_{lp,i}(k+1) = \left(1 - 2\pi f_{lp}\right)x_{lp,i}(k) + 2\pi f_{lp} I_i(k) \\ x_{hp,i}(k+1) = \frac{1}{2\pi f_{hp}+1} x_{hp,i}(k) + \frac{1}{2\pi f_{hp}+1}\left(x_{lp,i}(k+1) - x_{lp,i}(k)\right) \\ \bar{I}_{pb,i}(k) = x_{hp,i}(k) \end{cases} \quad (13)$$

where $f_{lp} = 0.0002$ and $f_{hp} = 0.0001$. When the absolute value of the resulting filtrated signal becomes greater than a certain value, the anode slippage is declared and the $\bar{I}_{pc,i}$ current is reinitialized.

4. Local Alumina Observer

In Figure 4 we show a schematic representation of a single anode observer. In the following section, we present the recursive equations at the base of the local alumina observer, then we present the application of the observer on real plant data.

4.1 Observer Design and Implementation

We define the anode dissolved alumina concentration and ACD of the i-th anode:

$$\begin{aligned} \widehat{w}_{d,i}(k) &= \widehat{w}_d(k) + \Delta\widehat{w}_{d,i}(k) \\ \widehat{ACD}_i(k) &= \widehat{ACD}(k) + \Delta\widehat{ACD}_i(k) + \hat{a}_{w,i}(k) \end{aligned} \quad (14)$$

where $\Delta\widehat{w}_{d,i}(k)$ is the difference between the i-th anodic dissolved alumina $\widehat{w}_{d,i}(k)$ and the *instrumental* dissolved alumina. The i-th anodic pseudo-ACD $\widehat{ACD}_i(k)$ is defined as the sum of three different components: the *instrumental* $\widehat{ACD}(k)$, the i-th pseudo-ACD difference $\Delta\widehat{ACD}_i(k)$ and the metal wave amplitude under the i-th anode $\hat{a}_{w,i}(k)$. We decided to separate the metal wave amplitude $\hat{a}_{w,i}(k)$ from the $\Delta\widehat{ACD}_i(k)$ estimation because the fundamental oscillation frequency of this phenomenon f_0 is known. Therefore, the observer is designed such that the f_w

frequency component of the i-th anode resistance is imputed to $\hat{a}_{w,i}(k)$. The physical modelling information other than the ones used in the alumina dissolution dynamics and the mass-balance equations are uncertain, therefore we propose the following model for a single anode:

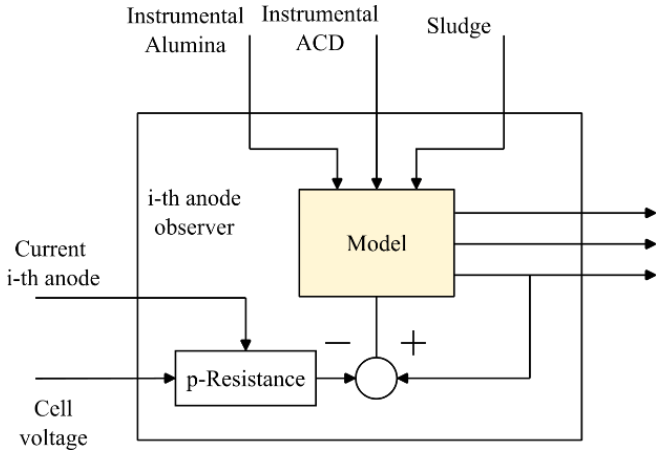

Figure 4. Schematic representation of the i-th anode observer.

$$\begin{cases} \dot{\widehat{\Delta w}}_{d,i}(t) = 0 \\ \dot{\widehat{\Delta ACD}}_i(t) = 0 \\ \dot{\hat{a}}_{w,i}(t) = w_0 \hat{v}_{w,i}(t) \\ \dot{\hat{v}}_{w,i}(t) = -w_0 \hat{a}_{w,i}(t) \\ \hat{R}_i(t) = N\left(\frac{k_1}{\hat{w}_{d,i}(t) - w_{ae}} + k_2 \hat{w}_{d,i}(t) + k_3 \widehat{ACD}_i(t) + k_4 + k_5(\hat{w}_{sl}(t) - w_{sl}^*) \right) \end{cases} \tag{15}$$

Where $w_0 = 2\pi f_0$ and f_0 corresponds to the fundamental frequency of the metal pad that depends on the dimensions of the cell under study. The measured output corresponds to the anode pseudo-resistance that is obtained using the pre-processed anode current presented in Section 3.1 using the following expression:

$$R_i(t) = \frac{V_{cell}(t) - k\_0}{\bar{I}_i(t)}. \tag{16}$$

We define the discrete state at the k instant of time $\Delta\hat{x}_i(k) = \left[\widehat{\Delta w}_{d,i}(k), \widehat{\Delta ACD}_i(t), \hat{a}_{w,i}(k), \hat{v}_{w,i}(k)\right]^T$. In discrete time, the system equation transforms to:

$$\begin{cases} \Delta\hat{x}_i(k+1) = A_l \Delta\hat{x}_i(k) \\ \hat{R}_i(k) = N\left(\frac{k_1}{\hat{w}_{d,i}(k) - w_{ae}} + k_2 \hat{w}_{d,i}(k) + k_3 \widehat{ACD}_i(k) + k_4 + k_5(\hat{w}_{sl}(k) - w_{sl}^*) \right) \end{cases} \tag{17}$$

where,

$$A_l = \begin{bmatrix} 1 & 0 & 0 & 0 \\ 0 & 1 & 0 & 0 \\ 0 & 0 & 1 & w_0 \\ 0 & 0 & -w_0 & 1 \end{bmatrix}. \tag{18}$$

As previously mentioned, to obtain the *instrumental* estimations we first apply the EKF on system (7). At each time instant, we update the current pre-processing to filter the low frequencies, exclude a current if its variance its bigger than a certain threshold and identify the anode slippage to re-initialize the anode pseudo-ACD. Then, the EKF is applied to system (17) to obtain the local

estimation for the anode with validated current. The local alumina observer algorithm is initialized and started together with the instrumental alumina observer. The convergence time to plausible estimation for the local alumina observer is of about 1 hour and 20 minutes.

4.2 Application to Industrial Aluminium Cells

In this section, we test the proposed observer on data collected from an industrial aluminium reduction cell. The algorithm is tested on two different periods: during a day without cell anomalies (normal day) and just before an anode effect. The estimation results are commented and their coherence with physical considerations is highlighted for the two different periods.

4.2.1 Normal Day

In Figure 5, we show the estimation overview during an anode-effect free period plotting: the feeding period, the measured and filtered pseudo-resistance, $\hat{w}_d$ with $\min_i(\{\hat{w}_{d,i}, i = 1, \dots N\})$ and $\max_i(\{\hat{w}_{d,i}, i = 1, \dots N\})$ dissolved alumina concentration and $\widehat{ACD}$ with $\min_i(\{\widehat{ACD}_i, i = 1, \dots N\})$ and $\max_i(\{\widehat{ACD}_i, i = 1, \dots N\})$.

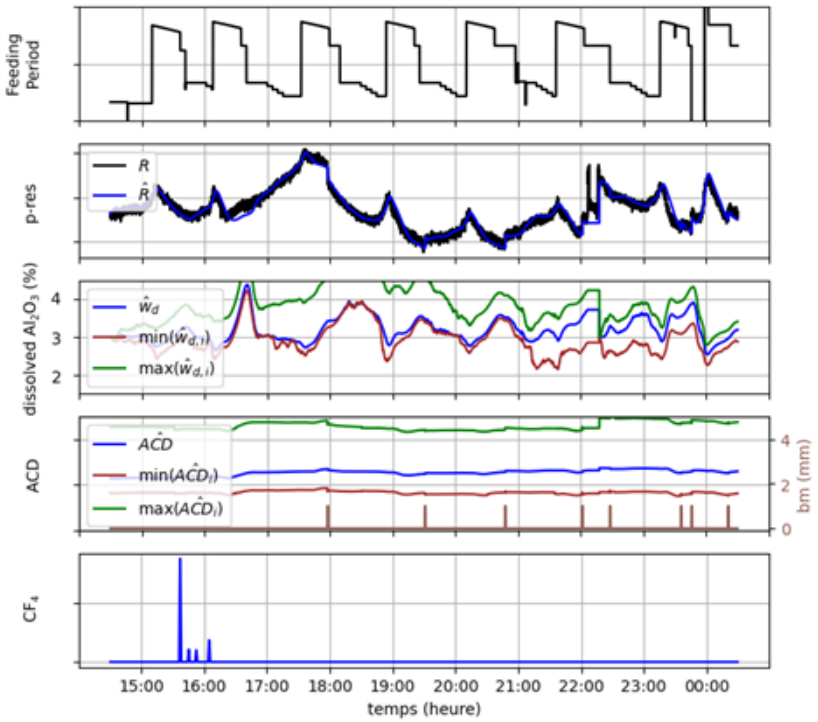

Figure 5. General overview of the estimation during the analysis period of a normal day.

We can remark that during analysed period the min alumina estimation stays away from the alert value of 2 %. This is coherent with the almost zero measured CF_4 during the overall period. In Figure 6(a) and 6(b) we show the estimation for the anodes 1 and 20, respectively. In these figures, we plot the anode current, the estimated variance, the anode pseudo-resistance, the estimated *instrumental* and anode dissolved alumina, the estimated *instrumental* ACD together with the anode pseudo-ACD and the beam movement. The anode 20 is an example of an anode with the tendency of having a lower concentration of alumina in opposition to anode 1. This can be observed in peaks difference in the anode pseudo-resistances: the sharper peaks of anode 20 are due to downside peaks of its anode current, while the peaks absence of anode 1 are due to upside peaks of its anode current. This is in accordance with the simulation results in Section 4.1 of [5].

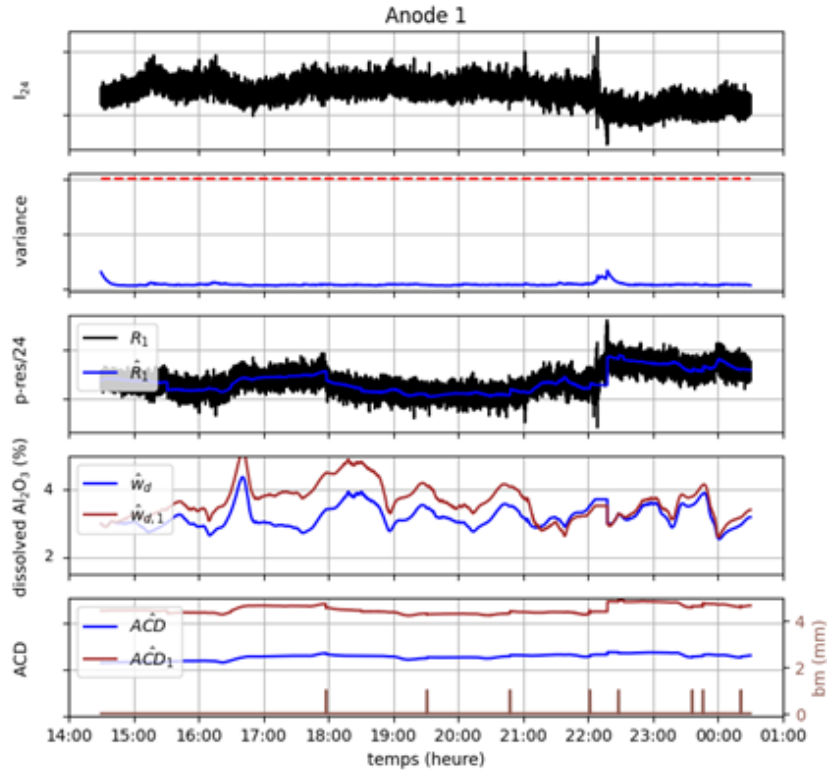

(a)

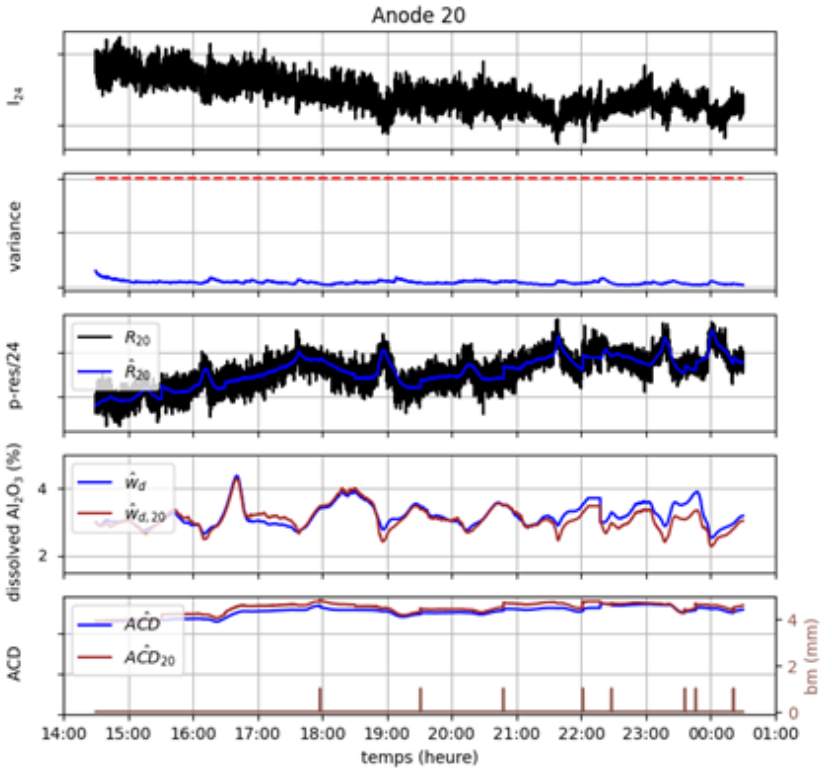

(b)

Figure 6. Alumina and ACD estimation compared to the *instrumental* ones. Anode 1 has in average more alumina than the *instrumental*, while anode 20 has in average less alumina than the *instrumental*.

4.2.2 Before Anode Effect

As in the previous section, in Figure 7 we show the estimation overview during a time interval just before an anode effect. Looking at the measured emitted CF_4, we can remark that during this period a first pseudo-anode effect happens at around 13:30 h while the anode effect happens at the end of the analysed period at around 16:00 h. We remark that during this period, the estimated *instrumental* alumina concentration does not suggest either the pseudo or the actual anode effect.

This happens because, in this case, the anode effect started locally from a single anode and then propagated to the overall cell. On the contrary, we can remark from Figure 7 that the $\min_i(\{\hat{w}_{d,i}, i = 1, \dots N\})$ suggests that the alumina has dropped for some of the anodes before the beginning of both cases. It is possible to appreciate that some minutes before the actual declaration of anode-effect, the $\min_i(\{\hat{w}_{d,i}, i = 1, \dots N\})$ alumina concentration was already under 2 % and monotonically decreasing. In Figure 8, we plot the estimation overview of the anode 24. The anode current drop before the first pseudo anode effect as well as before the actual anode effect suggests that anode 24 is one of the responsible of both. We remark that the estimated dissolved alumina concentration of anode 24 is coherent with the previous consideration.

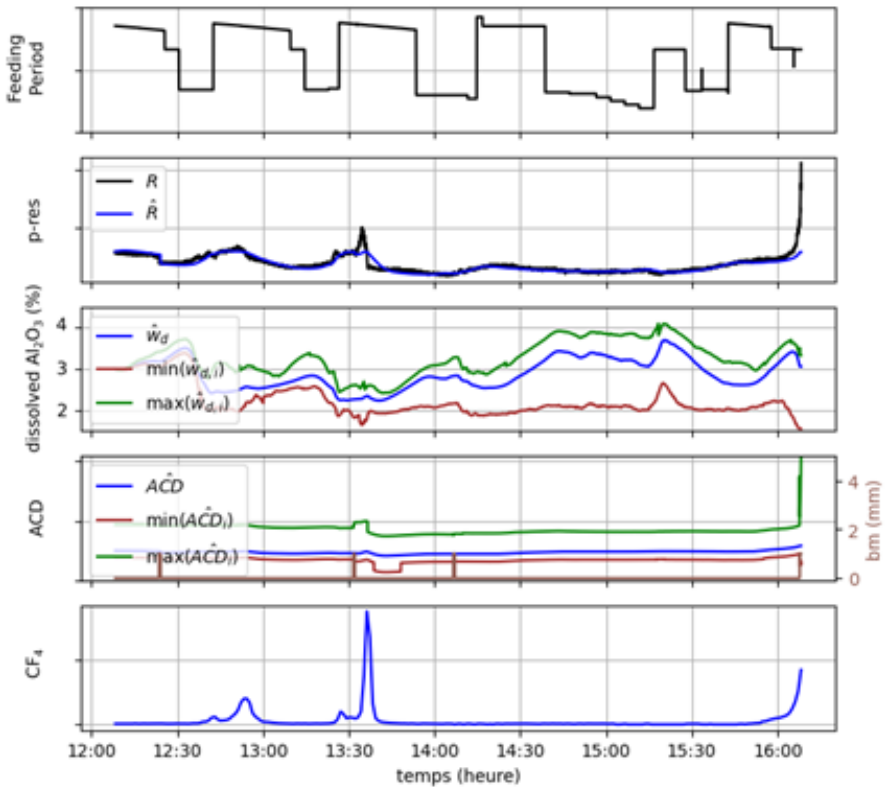

Figure 7. General overview of anode estimations during a period before an anode effect.

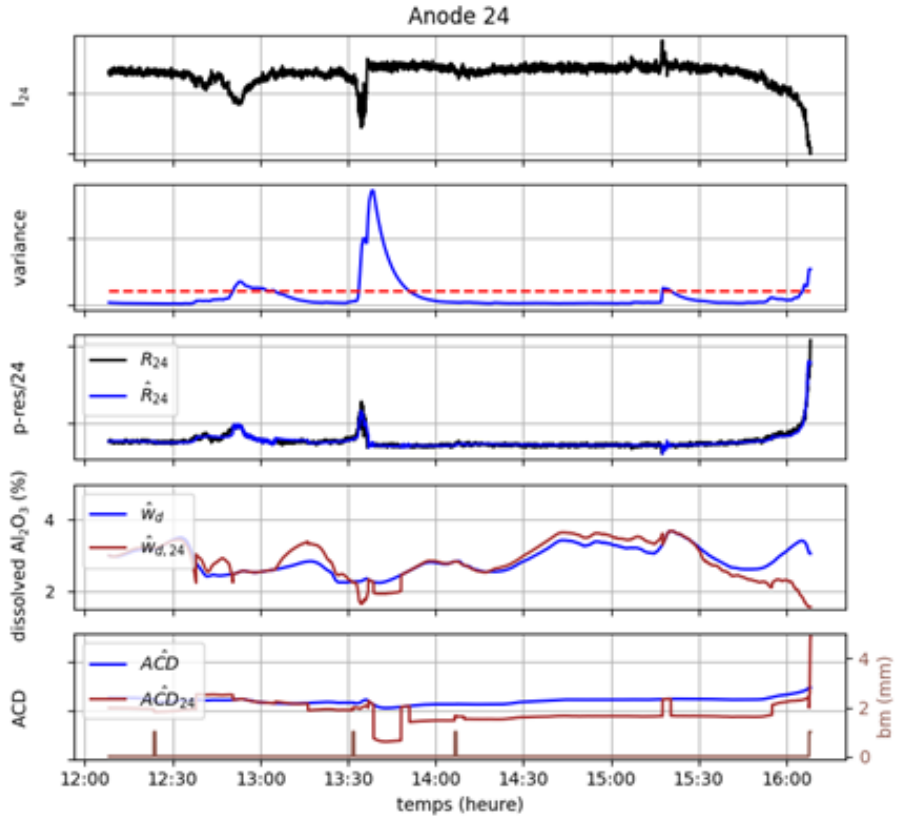

Figure 8. General overview of an estimation of the anode from which the anode effect started.

5. Conclusions and Future Perspectives

In this paper, a local alumina observer making use of the anode currents to correct the estimations has been presented. The proposed observation algorithm is composed by two different stages. The first stage estimates the *instrumental* dissolved alumina and *instrumental* ACD using the cell pseudo-resistance. The second stage estimates the difference between local and *instrumental* dissolved alumina and ACD making use of the anode pseudo-resistance. The anode pseudo-resistances are computed using the anode currents after a pre-processing stage that removes the frequencies of the non-modelled behaviours. To validate the proposed algorithm, it has been tested on data coming from an industrial aluminium cell on two different periods. The first period was during a normal day, while the second period was during a day with an anode effect. In absence of reliable direct measurements of dissolved alumina concentration, in both days we highlight the coherence of the estimations with the measured signals.

Possible future developments include the classification of the estimation results to relate them with abnormal behaviours of the cell. For example, this can be done using the One Class Support Vector Machine (OCSVM) or the Local Outlier Factor (LOF) 300 algorithms. Another possible future direction of research will be the use of the obtained estimations for control purposes. A step in this direction will be the study of the cell local estimation when a disbalanced feeding is applied. This will help understand how the cell distributes the dissolved alumina according to the feeding unbalancing.

6. References

1. Warren Haupin and Edward J. Seger, Aiming for Zero Anode Effect, *Light Metals* 2001, 767-773.
2. Jayson Tessier, Katie Cantin and David T. Magnusson, Investigation of Alumina Concentration Gradients Within Hall-Héroult Electrolytic Bath, *Light Metals* 2018, 515-522.
3. Yuchen Yao et al., Estimation of spatial alumina concentration in an aluminum reduction cell using a multilevel state observer, *AIChE Journal*, Vol. 63, No. 7, (2017), 2806-2818.
4. Yuchen Yao and Jie Bao, State and parameter estimation in Hall-Héroult cells using iterated extended Kalman filter, *IFAC-PapersOnLine*, Vol. 51, No. 21, (2018), 36-41.
5. Jing Shi et al., Multivariable feeding control of aluminum reduction process using individual anode current measurement, *IFAC-PapersOnLine*, Vol. 53, No. 2, (2020), 11907-11912.
6. Luning Ma et al., Estimation of the Spatial Alumina Concentration of an Aluminium Smelting Cell Using a Huber Function-Based Kalman Filter, *Light Metals* 2024, 464-473.
7. Andrea Mattioni et al., A step towards implementation of state observers in industrial aluminium smelters, *proceedings of 12th IFAC SAFE Processes Conference*, Ferrara, Italy, 4-7 June 2024, Paper 84.
8. Halvor Kvande et al., Pseudo resistance curves for aluminum cell control-alumina dissolution and cell dynamics, *Essential Readings in Light Metals*, Vol. 2, (2016), 760-766.
9. Xiangwen Wang et al., Development and Deployment of Slotted anode Technology at Alcoa, *Light Metals* 2007, 299-304.
10. Geoff Bearne, Derek Gadd and Simon Lix, The Impact of Slots on Reduction Cell Individual Anode Current Variation, *Light Metals* 2007, 305-310.
11. Cheuk-Yi Cheung et al., Characterization of individual anode current signals in aluminium reduction cells, *Industrial & Engineering Chemistry Research*, Vol. 52, No. 28, (2013), 9632-9644.